Thermal Analysis of Passively Cooled Hybrid CPV Module Using Si Cell as Heat Distributor

Juan F. Martínez, Marc Steiner, Maike Wiesenfarth, Stefan W. Glunz, and Frank Dimroth

***Abstract*—In this paper, we introduce a new kind of hybrid concentrator photovoltaic module that is capable of harvesting direct and diffuse irradiance. The concept, denominated EyeCon, uses a Fresnel lens to concentrate direct irradiance onto a primary III–V four-junction solar cell. Directly underneath, a large-area silicon cell is stacked and used as a secondary conversion material for diffuse irradiance while also acting as a heat distributor. This paper focuses on determining the feasibility of this concept based on the evaluation of the thermal behavior of both cells. Such assessment is performed using finite element analysis, indoor infrared thermography, and outdoor measurements under real concentrator operating conditions. The results reveal that under an ambient temperature of 25 °C and a geometric concentration of 226 × 900 W/m^2 plus 100 W/m^2 of diffuse irradiance, the concentrator III–V and silicon cell temperatures do not increase beyond 80 °C and 60 °C, respectively. Thus, our analysis shows that the silicon can be used simultaneously as a heat distributor and a solar cell.**

***Index Terms*—Direct plus diffuse irradiance, hybrid concentrator photovoltaic (CPV) on silicon (Si) module, silicon as heat distributor, III–V and concentrator PV.**

I. Introduction

Improving photovoltaic conversion of solar energy is a key aspect of promoting the transformation of our fossil fuel dependent systems into renewable and sustainable ones. In this sense, concentrator photovoltaic (CPV) technology based on III–V multi-junction solar cells for terrestrial applications offers the highest conversion efficiency possible [1], [2], 43.4% today [3]. However, their performance can be severely affected in the case of high cell operating temperatures caused by concentration [4]. For this reason, CPV modules require effective thermal management in order to retain their high efficiency and reliability [5]–[8]. Furthermore, the use of concentrating optics limits their conversion ability to direct normal irradiance (DNI). This means that they are unable to capture full global normal irradiance (GNI) to also generate power with the diffuse part of the solar spectrum. This diffuse component can represent 10% to over 30% of unused solar resource even in locations with high

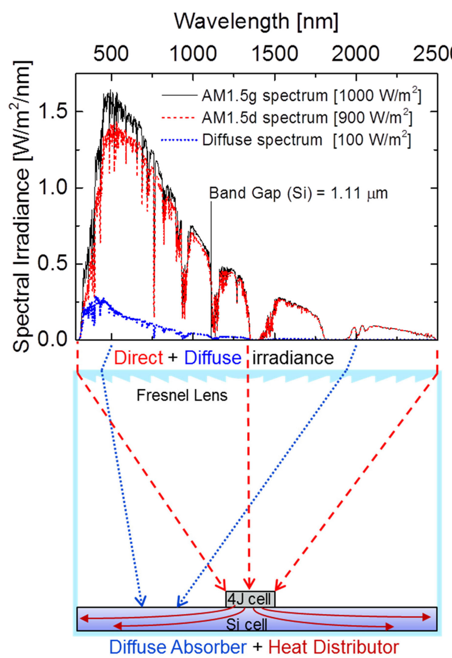

Fig. 1. Top: Standard solar resource on earth (black) composed of diffuse (blue dotted) and direct (red dashed) spectra. Bottom: Diagram of the EyeCon concept where a Fresnel lens concentrates DNI onto a 4J cell, while a Si cell absorbs diffuse irradiance and also acts as a heat distributing substrate.

direct irradiation (>2000 kWh/(m^2·a)) [9]. This issue may be circumvented by integration of a secondary large-area solar cell that absorbs and converts diffuse irradiance at low cost. Fig. 1 shows that silicon (Si) is a suitable material to do so because its band gap energy (1.11 μm) [10] is lower than most of the diffuse spectrum available. In addition, the Si solar cell industry has outstandingly driven down the price of 6″ monocrystalline Si cells ($0.87 per cell—June/2018) [11] while pushing their efficiency (26.7%) [12] closer to the theoretical limit. For these reasons more than ever, integration at the module level of silicon and concentrator III–V multi-junction solar cells has attracted the attention of many research groups in order to boost photovoltaic conversion [13]–[17]. The main idea of enhancing a conventional CPV module with a secondary low-cost solar cell was first patented by Benitez *et al.* in a four-terminal configuration [13] and then by Meitl *et al.* in a two-terminal fashion [14]. Today, different approaches and architectures aiming to implement the aforementioned idea can be found in the literature. For instance, in 2014, Yamada and Okamoto [15] introduced a CPV mono-module (476×) that uses a Fresnel lens (144 cm^2)

Manuscript received June 15, 2018; revised September 10, 2018; accepted October 14, 2018. The Ph.D. work of J. F. Martínez was supported in part by the National Council of Science and Technology and in part by the Mexican Secretary of Energy. *(Corresponding author: Juan F. Martínez.)*

The authors are with the Fraunhofer Institute for Solar Energy Systems ISE, D-79110 Freiburg, Germany (e-mail: juan.francisco.martinez.sanchez@ise.fhg.de; marc.steiner@ise.fhg.de; maike.wiesenfarth@ise.fhg.de; stefan.glunz@ise.fhg.de; frank.dimroth@ise.fhg.de).

Color versions of one or more of the figures in this paper are available online at http://ieeexplore.ieee.org.

Digital Object Identifier 10.1109/JPHOTOV.2018.2877004

This article has been accepted for inclusion in a future issue of this journal. Content is final as presented, with the exception of pagination.

to concentrate DNI onto a triple-junction solar cell. Above this cell, they integrated a large-area crystalline Si cell that collects diffuse irradiance, while it allows concentrated light to penetrate through a hole in its surface. The four-terminal mono-module generated 44% more power than the CPV part alone when the DNI to GNI ratio (DNI/GNI) was 0.6. Then in 2016, Yamada and Hirai [16] investigated the performance of a 200× miniature CPV module that combines III–V triple-junction and bifacial Si solar cells. Their configuration packages 16 CPV cells onto a copper pattern fabricated on a glass substrate. Underneath the substrate, a laminated bifacial cell collects diffuse light from front and rear. Furthermore, they used a full polymethyl methacrylate lens array (32.5 cm^2) as primary optics combined with a reflective secondary optical element. Their four-terminal mini-module generated 39% more power than its equivalent without a bifacial Si cell when DNI/GNI > 0.75, and 63% when $0.4 <$ DNI/GNI < 0.5. Also, in 2016, Lee *et al.* [17] contributed with their micro-CPV module (∼1000×) that uses 660 triple-junction cells and 93 laser-cut Si interdigitated back contact (IBC) cells. All cells are mounted onto a copper backplane under an inward-facing array of plano-convex lenses (0.303 m^2) as primary optics. Additionally, refractive ball lenses are used as secondary optics. In their four-terminal prototype, the power output of the CPV part alone was increased 3.4% even under very high DNI/GNI (0.924) conditions. These examples show that hybridization has the potential to boost conventional CPV power output between 3% and 60% depending on the design and the DNI/GNI ratio.

In Fig. 1, we introduce the EyeCon concept, a new hybrid CPV module developed at Fraunhofer ISE. The concept uses a Fresnel lens to concentrate DNI (red dashed) onto a III–V four-junction cell, while a large-area Si cell harvests diffuse irradiance (blue dotted) and also acts as a heat distributing substrate. The CPV cell is mechanically stacked directly on the top of silicon to facilitate heat transfer. However, a dielectric adhesive is used between the cells in order to avoid the need for current or voltage matching. Hence, the concept is a four-terminal architecture. Lastly, the cell stack is laminated onto a glass baseplate with ethylene-vinyl acetate (EVA). This dual use of silicon aims at increasing power output while leveraging its added cost by replacing the metal heat sink used in conventional CPV modules. Nevertheless, silicon's ability to work as a heat distributor without thermally compromising CPV and its own performance still needs to be assessed. For this reason, the paper focuses on investigating the thermal behavior of the concept using finite element simulation, indoor infrared thermography (IRT), and outdoor testing of a submodule under real concentrator operating conditions.

II. Finite Element Model (FEM)

The FEM used for thermal simulations has three main parts: the three-dimensional (3-D) CAD drawing, the heat loads, and the boundary conditions. In Fig. 2, we show the exploded view of the smallest element of symmetry (1/4) of the CAD drawing used for simulation. It consists of seven stacked components: CPV cell, solder, back contact, dielectric adhesive, silicon cell, lamination, and baseplate.

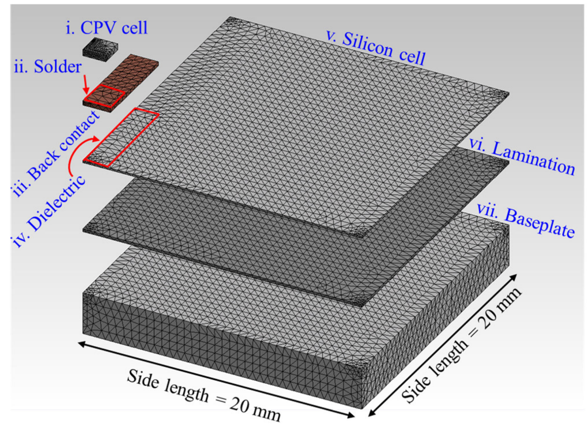

Fig. 2. Exploded view of the FEM's smallest element of symmetry (1/4). Components i, iii, v, vi, and vii are represented as solid bodies, whereas components ii and iv are implemented as thermal resistances due to their thin or variable thickness. The mesh has 94 188 nodes with triangular elements.

TABLE I
Geometrical and Physical Properties of the FEM

Component	Material	Size mm x mm	t µm	k W/(m·K)	ε a.u.
CPV cell	GaAs	1.6 x 1.6	450	55***	0.69**
Solder	SnAgCu	1.6 x 1.6	20	58*	n/a
Back Contact	Cu-Ni	2 x 6	300	390*	0.3*
Dielectric	var	2 x 6	var	var	n/a
Silicon cell	Si	20 x 20	150	130***	0.67**
Lamination	EVA	20 x 20	200	0.34*	n/a
Baseplate	Glass	20 x 20	3000	0.75*	0.96*

Thermal conductivities and emissivities are given at room temperature. Sources: Jaus [18]*, k-space [19]**, and Ioffe [20]***.

The required geometrical and physical properties, such as size, thickness (t), thermal conductivity (k), and emissivity (ε), for the thermal steady-state solution are given in Table I.

In order to enable comparison with experimental measurements, the model was simulated in open circuit to approximate the thermal condition that occurs outdoors during intermittent *I–V* sweeping. Furthermore, the absorbed DNI and diffuse irradiance constitute the thermal loads to be implemented on the model's surface as radiant heat fluxes. For this, the radial concentration profile $C(r)$ of the Fresnel lens ($A_{\text{lens}} = 16$ cm^2) used outdoors was measured under narrow bandwidth red light (622 nm, FWHM 20 nm) [21]. The result is the following equation, a bell-shaped curve that scales with DNI to represent the heat flux on the CPV cell surface $G_c(r)$ due to a geometric concentration ($C_{\text{geo}} = A_{\text{lens}}/A_{\text{CPV}}$) of 226×:

$$G_c\left(r\right) = \text{DNI} \cdot \left(1 - \rho_{\text{cpv}}\right) \cdot C\left(r\right) \tag{1}$$

where r is the radial vector of the CPV cell and ρ_{cpv} is its reflectance loss (0.10) taken from [18]. Note that the lens optical efficiency ($\eta_{\text{opt}} = 0.874$) is accounted for in $C(r)$. In contrast, diffuse irradiance on both cell surfaces was assumed to be homogeneous and its corresponding heat flux G_d is calculated by

$$G_d = \left(\text{GNI} - \text{DNI}\right) \cdot \left(1 - \rho_{\text{si}}\right) \tag{2}$$

where ρ_{si} is the reflectance loss of the Si cell (0.10) taken from [22]. In Fig. 3, we present the radial heat load profile calculated

This article has been accepted for inclusion in a future issue of this journal. Content is final as presented, with the exception of pagination.

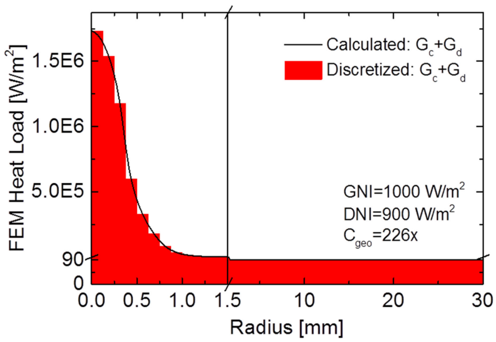

Fig. 3. Calculated (black line) and discretized (red area) radial heat load profile based on the AM1.5g spectrum. The geometric concentration C_{geo} is 226×. Note the *y*-axis change in scaling at 100 W/m^2 and the *x*-axis change in scaling at 1.5 mm.

TABLE II
BOUNDARY CONDITIONS OF THE FEM

Exposed surfaces	Heat Exchange mechanism	Exchanging media	$\bar{h}$ W/(m^2·K)	T_{media} °C
Top	Convection	Air in module	7	50
Top	Radiation	Lens	f(T_{surf})	35
Bottom	Convection	Ambient air	9	25
Bottom	Radiation	Ground	f(T_{surf})	25

Convective heat exchange coefficients ($\bar{h}$) as well as all media temperatures (T_{media}) were taken from [18].

with (1) and (2) for the AM1.5g spectrum (GNI $=$ 1000 W/m^2, DNI $=$ 900 W/m^2). The discretized $G_c(r)$ is implemented on the CPV cell surface as a series of 12 concentric rings of equal width, whereas G_d is applied uniformly on both cells.

The boundary conditions of the FEM are defined at the exposed top and bottom surfaces by the average heat exchange coefficients ($\bar{h}$) and the temperatures of the media they interact with (T_{media}). In Table II, we present a summary of the boundary conditions used in our model. These were taken from the work of Jaus [18] where he validated that internal and external convection coefficients of 7 and 9 W/m^2·K reduce the error between simulation and measurement below 1 K for a conventional CPV module with a passive metal heat distributor. Additionally, he measured the temperature of the lens and the air inside the module to be 36.9 $\pm$ 2.4 °C and 50.7 $\pm$ 2.5 °C when DNI $=$ 850 W/m^2, T_{amb} $=$ 24.4 $\pm$ 2.5 °C, and $V_{\mathrm{wind}} = 0.57$ m/s.

The implementation of these boundary conditions into our model allows us to simplify the 3-D drawing by removing the lens and frame bodies if we assume a fixed temperature of the lens and air inside the module. This also requires assuming effective convection coefficients for top and bottom surfaces. Together, these assumptions proved to be adequate given the strong correlation between simulation and experimental data presented in the next sections. Computing time and resources were also significantly reduced.

III. THERMAL SIMULATION

A. *Temperature Distribution on CPV and Si Cell Surface*

Thermal simulation of the FEM using the heat load profile in Fig. 3 and a moderate dielectric adhesive thermal resistance ($R_d = t/k = 150\,\mathrm{mm}^2$·K/ W) yields the cell temperature profiles in Fig. 4. Although small in size, the CPV cell describes a Gaussian profile (red triangles) on its surface due to the intensely concentrated heat flux in the center and its finite thermal conductivity. On the other hand, the silicon cell temperature (blue circles) decays logarithmically along its radius as is expected of a thin plate conducting heat away from its center [23]. Both the CPV and Si cell present hot spots in their centers, 84.7 °C and 72.7 °C; however, from now on we will refer to the top surface average, 77.8 °C and 63.6 °C, because it is more representative of the effective p–n junction temperature. The 3.5 K gradient between CPV and Si cells is due to the dielectric adhesive thermal resistance.

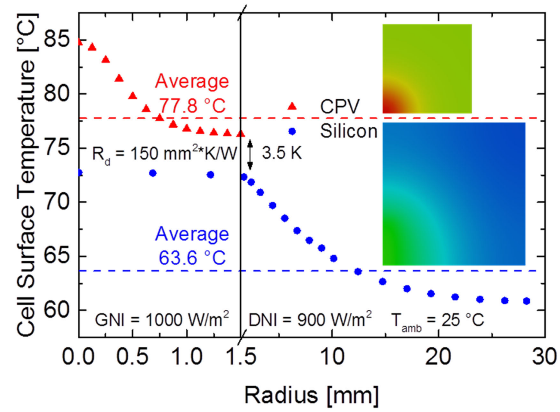

Fig. 4. Simulated CPV (red triangles) and Si (blue circles) cell temperature profile from center to corner. The horizontal dashed lines depict the cells average temperatures. Thermal resistance of the dielectric adhesive is 150 mm^2·K/W. Note the *x*-axis change in scaling at 1.5 mm. Insets: CPV and Si cell thermograms.

B. *CPV Cell Temperature vs. Thermal Resistance of Dielectric*

In order to reduce the CPV cell temperature, the overall thermal resistance of the module needs to be minimized. This section investigates the influence of the dielectric adhesive thermal resistance (R_d) because it is crucial in enabling silicon to perform as a heat distributor. Also, because its value varies over four orders of magnitude, the right material has to be selected. Such broad range comprehends commercially available dielectrics like ceramic substrates, high thermal conductivity pre-pregs, epoxy, or acrylic adhesives that are filled with Ag or ceramic and insulating flame retardant composites, like FR-4. In Fig. 5, we show in a semi-log plot how the CPV cell temperature rises 24 K when R_d increases from 0.1 to 1000 mm^2·K/W. This underlines the importance of selecting a dielectric with R_d not greater than 225 mm^2·K/W for the CPV cell to operate at a reasonable temperature, i.e., <80 °C. However, since cheap direct soldering cannot be used due to the lack of electrical isolation of the circuits, an isolating adhesive is necessary, but choosing an adhesive with R_d lower than 35 mm^2·K/W is not required because it elevates material cost without significantly lowering CPV temperature. We have chosen a dielectric thermal tape of ceramic-filled acrylic (R_d $=$ 150 mm^2·K/ W) to assemble the prototypes for indoor and outdoor tests.

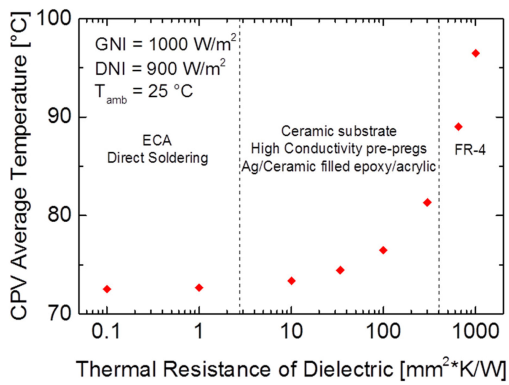

Fig. 5. Simulated CPV cell average temperature as a function of logarithmic thermal resistance of the dielectric adhesive. The vertical dashed lines divide the different kinds of adhesives into three groups: highly electrically and thermally conductive (left), electrically insulating but thermally conductive (center), and electrically insulating and poorly thermally conductive (right).

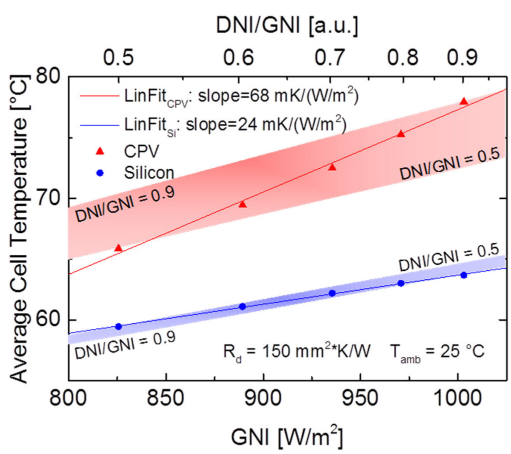

Fig. 6. Simulated CPV (red triangles) and Si (blue circles) cell average temperature as a function of GNI and DNI/GNI (top x-axis). Solid lines depict the linear fits applied to both cells. Shaded bands show the temperature fluctuation at every GNI level if DNI/GNI varies between 0.5 and 0.9. Thermal resistance of the dielectric adhesive is 150 mm^2·K/W.

C. CPV and Si Cell Temperature vs. Irradiance

We have investigated the thermal behavior of the hybrid CPV module under the standard AM1.5g spectrum. Now, we present its behavior under a realistic range of DNI/GNI values (0.5–0.9) encountered outdoors and an ambient temperature of 25 °C. For this purpose, we used SMARTS2 to extract broadband GNI and DNI while increasing the aerosol optical depth of the typical mid-latitude summer atmosphere (45 N) [24]. The result is a decrease in GNI, DNI, and DNI/GNI. As shown in Fig. 6, the FEM yields a linear increase of CPV (red triangles) and Si (blue circles) cell temperatures with GNI at a rate of 68 and 24 mK per W/m^2 (linear fits), respectively. Therefore, we can expect the CPV and Si cells to operate 12 and 4.3 K hotter, respectively, when DNI nearly doubles, but GNI only increases 20%. This 3:1 ratio in temperature increment reflects the significant impact of DNI/GNI on the CPV cell temperature. Moreover, as depicted by the shaded bands, the average CPV and Si cell temperature fluctuates up to 5.5 and 1 K within its band's edges where DNI/GNI varies between 0.5 and 0.9 at any GNI level.

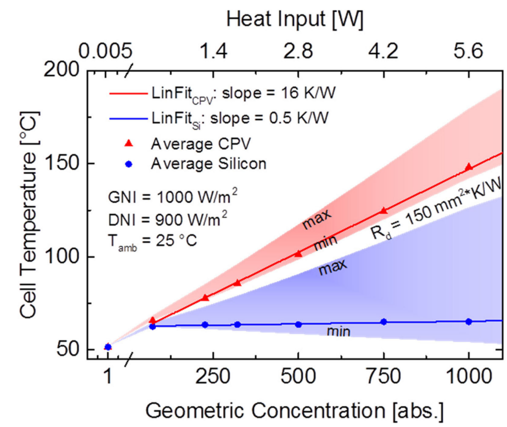

Fig. 7. Simulated CPV (red triangles) and Si (blue circles) cell average temperature as a function of C_{geo} or heat input. Solid lines depict the linear fits applied to both cells above 72×. The shaded bands show the maximum and minimum cell temperature. The AM1.5g spectrum (DNI = 900 W/m^2 and diffuse irradiance = 100 W/m^2) was used as the input heat load and the thermal resistance of the dielectric adhesive is 150 mm^2·K/W. Note the x-axis change in scaling at 2× or 0.01 W.

D. CPV and Si Cell Temperature vs. Geometric Concentration

Increasing geometric concentration is a way to reduce the cost of CPV systems; therefore, this section investigates the thermal effects of linearly increasing the concentrated heat flux $G_c(r)$ of the AM1.5g spectrum according to geometric concentration. For the analysis, the lens aperture and the Si cell surface area were increased proportionally, whereas the CPV cell size was fixed at 7.07 mm^2. In Fig. 7, we show that the CPV and Si cells heat up 16 and 0.5 K per Watt of heat input. At this rate, the CPV cell already operates above 100 °C at 500×; therefore, it is not recommended to concentrate more than 2.8 W onto one concentrator solar cell. On the other hand, the average Si cell temperature at the same concentration level remains nearly constant (64 °C). However, as depicted by the blue shaded band, the concentrated heat in the CPV cell causes an intense center hot spot ($T_{\max} > 85$ °C) that decreases performance and degrades the EVA lamination [25]. At the same time, the minimum temperature of the Si cell decreases with concentration because its convective and radiative thermal resistances decrease with the surface area, while the conductive one increases. This yields a more severe hot spot and slightly colder edges. On the contrary, reducing the concentration to 1×, which is the limiting case of the FEM due to its boundary conditions, brings both cell temperatures (51 °C) to the thermal equilibrium temperature of the air inside the module. Additionally, we can observe in the gap between bands how the temperature gradient introduced by R_d increases 4.2 K from 226× to 500×. To mitigate this effect, R_d should be reduced to 25 mm^2·K/W.

IV. Infrared Thermography (IRT)

In this section, we present the IRT results of the temperature profile on the Si cell surface as well as the temperature dependence of the CPV cell with DNI. For this purpose, we symmetrically stacked a 3 × 3 array of chip resistor assemblies on the top of a 125 mm × 125 mm Si IBC cell using a dielectric

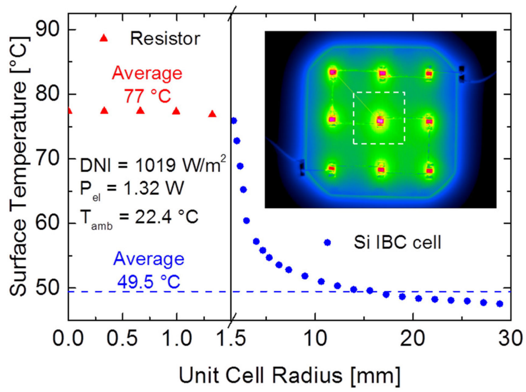

Fig. 8. Measured temperature profile of the resistor and Si IBC cell surface along the unit cell radius under DNI = 1019 W/m^2 or P_{el} = 1.32 W. Note the x-axis change in scaling at 1.5 mm. Inset: Measured thermogram of the prototype surface temperature. White dashed square depicts the unit cell.

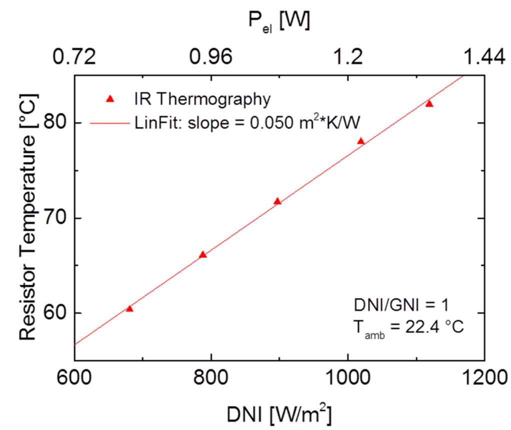

Fig. 9. Measured temperature of the center resistor (red triangles) as a function of equivalent DNI or P_{el} when T_{amb} = 22.4 °C. Red solid line is the linear fit to the IRT measurements and the slope represents the equivalent CPV cell thermal resistance to ambient.

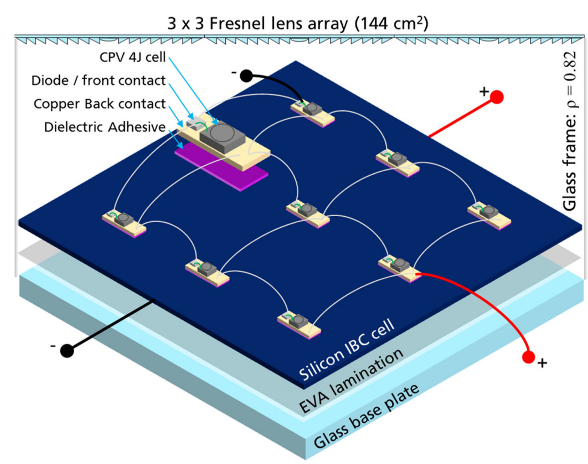

Fig. 10. Diagram of the EyeCon submodule used for outdoor testing. Array of 3 × 3 CPV SCAs is adhered on a 125 mm × 125 mm Si IBC cell with a thermal tape. SCAs are interconnected by heavy wire bonding to form three series strings of three cells in parallel. Prototype is enclosed by the Fresnel lens plate, the glass baseplate, and a mirror glass frame.

thermal tape (R_d = 150 mm^2·K/ W). Each assembly consists of a 5 mm × 6 mm chip resistor (1.5 Ω) soldered onto a small copper substrate (5 mm × 12 mm). When the current flows through these nine series interconnected resistors, they emulate the input heat load from concentrated DNI that would impinge on the CPV cells outdoors. In this manner, the thermal behavior of the EyeCon concept can be approximated and recorded in the laboratory. For the experiment, the emissivity setting of the IR camera was set to 0.87, because it yielded an agreement within ±2 K with contact probe measurements. Additionally, diffuse irradiance was neglected and DNI input was calculated using

$$\mathrm{DNI} = P_{\mathrm{el}} \,/\, [A_{\mathrm{uc}} \cdot (\eta_{\mathrm{opt}} - \rho_{\mathrm{cpv}})] \quad (3)$$

where P_{el} is the electric power applied to each resistor, and A_{uc} is the area of the unit cell (16 cm^2). The thermogram in the inset in Fig. 8 shows the temperature distribution on the prototype's surface for an equivalent DNI input of 1019 W/m^2 that corresponds to a geometric concentration of 226× or 1.25 W per resistor. In this case, we observe that the center resistor reached an average temperature of 77 ± 2 °C and that the profile on the Si IBC cell decays logarithmically as predicted before by simulation, in Fig. 4, with an average of 49.5 ± 2 °C. Although the simulated outdoor conditions differ slightly compared to those in the laboratory, both results are within the uncertainty of the measured resistor temperature. In the following experiment, we used the resistor temperature as an indicator for the CPV cell average value.

In order to experimentally establish the temperature response of the CPV cell on the incident irradiance, we performed a variation of the input electric power P_{el} and recorded the temperature of the center resistor under a thermal steady state. In Fig. 9, we plot its temperature (red triangles) as a function of equivalent DNI or P_{el}. As expected from simulation, this relationship is linear (solid line), and by the electro-thermal analogy [23], we extracted the equivalent thermal resistance of the CPV cell to ambient from the slope to be 0.050 m^2·K/W. This value is 16% higher than the one simulated in Fig. 6 (0.043 m^2·K/W) for the case where DNI/GNI = 0.9 because the IRT experiment was conducted under DNI/GNI = 1; thus, a larger slope is in order.

V. Outdoor Testing Under Real Concentrator Operating Conditions

Besides thermal simulation and IRT, the temperature behavior of the CPV and Si cells was investigated under real outdoor concentrator operating conditions. For this purpose, we built the submodule shown in Fig. 10. The cell stack is made of nine CPV solar cell assemblies (SCAs) attached with a dielectric thermal tape to the surface of a 125 mm × 125 mm Si IBC cell. Each SCA consists of a III–V four-junction cell (Ø = 3 mm) and a bypass diode soldered onto a small copper substrate (4 mm × 12 mm) that functions as a back contact. Thin-wire bonds interconnect the cell with the diode and the diode's anode is used as a front contact. The SCAs interconnection is done via heavy-wire bonding in a configuration of three series strings of three cells in parallel. The cell stack is laminated with EVA to a 3-mm-thick glass plate where it is enclosed by a 3 × 3 Fresnel lens array (144 cm^2) and a surrounding glass frame. The latter has a mirror finish (ρ = 0.82) in order to reproduce the optical boundary that would exist in a larger module.

TABLE III
REFERENCE PARAMETERS OF THE HYBRID CPV MODULE

Cell/s	I_{SCr} A	V_{OCr} V	β_r mV/K	α_r mA/K	δ_r % /K	N_s a.u.
9 CPV 4J	0.419	12.081	-20.1	-0.1	-0.064	3
1 Si IBC	0.870	0.608	-2.0	+0.2	-0.051	1

The reference conditions for the CPV array are 23 °C and 226 × 900 W/m^2, and for the Si IBC cell, 25 °C and 150 W/m^2. α_r and δ_r are the I_{SC} and efficiency temperature coefficients under the reference conditions.

Testing was performed at our outdoor facility in Freiburg, Germany, between June and August 2017. The submodule was mounted on a dual-axis sun tracker, while the meteorological (ambient temperature T_{amb} and wind speed V_{wind}), spectral (GNI and DNI), and *I–V* characteristics were recorded every 15 s. After filtering the data, we kept over 2000 entries. Based on these measurements, we used Muller's [26] approach to calculate the effective operating temperature T of our CPV array (where cells on the edge of the array operate at a lower temperature) and Si IBC cell (which has an inhomogeneous temperature profile). The method uses

$$T = (V_{\text{OC}} - V_{\text{OC}r} + \beta_r \cdot T_r) \bigg/ \left[N_s \cdot \frac{n \cdot k}{q} \cdot \ln\left(\frac{I_{\text{SC}}}{I_{\text{SC}r}}\right) + \beta_r\right] \tag{4}$$

where V_{OC} and I_{SC} are the outdoor measured open-circuit voltage and short-circuit current, $V_{\text{OC}r}$, $I_{\text{SC}r}$, and β_r are the reference open-circuit voltage, short-circuit current, and V_{OC} temperature coefficient under the reference irradiance, 226 × 900 W/m^2 for the CPV array and 150 W/m^2 for the Si IBC cell, defined by its level during the outdoor thermal transient measurements, T_r is the reference temperature at which the dark *I–V* curve of the CPV array (23 °C) and the light *I–V* curve of the Si IBC cell (25 °C) were measured, N_s is the number of cells interconnected in series, n is the diode ideality factor based on the cell's number of junctions (1 and 4), $k = 1.380 \times 10^{-23}$ J/K is Boltzmann's constant, and $q = 1.602 \times 10^{-19}$ °C is the elementary charge. Table III summarizes the measured reference parameters of the hybrid CPV module.

In order to obtain a useful relationship to predict both cell temperatures, we adapted Faiman's linear model [27] to correlate T, T_{amb}, GNI, and V_{wind}. The following equation is the expression that results from exchanging the wind-dependent thermal conductance for a wind-dependent thermal resistance R_w:

$$(T - T_{\text{amb}})/\text{GNI} = R_w = R_{\text{ss}} + r_{\text{conv}} \cdot V_{\text{wind}} \tag{5}$$

where the intercept R_{ss} represents the steady-state thermal resistance and the slope r_{conv} accounts for the variation in convective thermal resistance due to wind speed (5 min average). As depicted in Fig. 11, the thermal resistance of both cells (scatter plots) decreases inversely proportional to V_{wind}.

If we solve for T in (5) while applying the conditions used in simulation, $V_{\text{wind}} = 0$ m/s, $T_{\text{amb}} = 25$ °C, and GNI = 1000 W/m^2, we obtain the CPV array operating at 77 ± 3 °C, where both the simulated FEM result in Fig. 4 (77.8 °C) and the IRT measurement in Fig. 9 (79.2 ± 2 °C) are within the model uncertainty. At the same time, the Si IBC cell operates

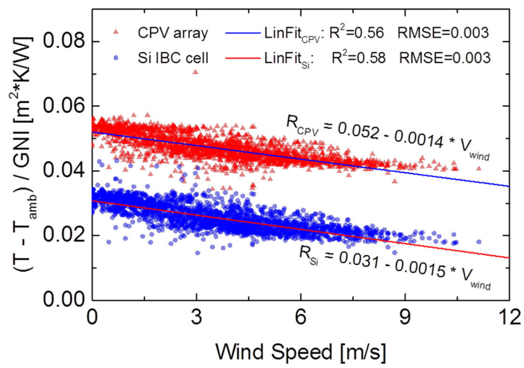

Fig. 11. Experimentally obtained CPV array (red triangles) and Si cell (blue circles) thermal resistance as a function of wind speed. The solid lines are the corresponding linear fits where the intercept is the steady-state thermal resistance and the slope represents the variation in convective thermal resistance due to wind speed.

at 56 ± 3 °C where the IRT measurement (49.5 ± 2 °C + (25 – 22.4) °C) corrected from 22.4 °C to 25 °C ambient temperature is within the uncertainty boundaries, while the simulated Si cell temperature (63.6 °C) is 4.6 °C above them. Hence, we can say that our FEM accurately predicts the CPV cell temperature, whereas it overestimates that of the Si cell. Nevertheless, both temperatures decrease 1.4 K for every m/s increment in wind speed. The uncertainty of the thermal resistance model is explained by the DNI/GNI variation between 0.5 and 0.92 during GNI progression from 400 to 1100 W/m^2, as previously described by the simulation in Section III-C.

The outdoor steady-state thermal resistance of the CPV array based on variable DNI/GNI is in agreement within 4% to the indoor IRT value obtained at DNI/GNI = 1. For comparison with conventional CPV module technology, we refer to the work of Siefer and Bett [28] where they calculated 0.040 m^2·K/W as the thermal resistance of a submodule using copper substrates and Fresnel lenses of the same size (16 cm^2) with comparable optical efficiency (0.85). This indicates that under the former conditions and DNI/GNI = 0.9, the CPV array in our proposed hybrid module would be 16 K hotter. This temperature difference represents a 1% loss in DNI conversion efficiency, which is easily compensated by the additional power generated in the Si cell. Other losses due to low and inhomogeneous illumination shall be investigated in future work; however, we expect the Si cell to have good performance outdoors. In addition, as DNI/GNI drops below 0.9, the power loss of the CPV array due to temperature decreases relative to GNI, whereas the Si cell contribution from diffuse irradiance increases. Electrical performance of the EyeCon concept can be found in [29].

VI. SUMMARY AND CONCLUSION

This paper investigates the thermal feasibility of using a silicon solar cell as the heat distributing substrate and diffuse irradiance converter of a hybrid CPV module. Such dual use of silicon is intended to leverage its extra cost by replacing the metal heatsink used in conventional CPV modules while increasing power output. Investigation of the CPV and silicon cell thermal behavior was performed using finite element simulation, indoor IRT, and outdoor measurements under real concentrator operating conditions.

Thermal simulation under $T_{\mathrm{amb}} = 25\,^{\circ}\mathrm{C}$, DNI $= 900$ W/m^2, diffuse irradiance $= 100$ W/m^2, and $C_{\mathrm{geo}} = 226\times$ revealed the following.

1) Due to concentration, the radial temperature distribution on the CPV cell surface follows a Gaussian profile, whereas that on the silicon cell decays logarithmically.
2) The distributed thermal resistance of the dielectric adhesive between CPV and silicon cells should not exceed 225 mm^2·K/W in order to keep their respective temperatures below 80 °C and 60 °C.
3) Both cell temperatures respond linearly to GNI; however, DNI/GNI introduces a fluctuation of 5.5 and 1 K, respectively.
4) The CPV cell operates above 100 °C at $C_{\mathrm{geo}} = 500\times$ (2.8 W) and the Si cell presents a 90 °C center hot spot.

In this sense, micro-CPV is an alternative path to explore in order to achieve lower cell operating temperatures at high geometric concentration.

Indoor IRT of a prototype assembly confirmed the logarithmically decaying temperature profile on the silicon cell surface and the linear relationship of the CPV cell temperature with DNI.

Outdoor measurements of a submodule yielded a linear model of thermal resistance as a function of wind speed that predicts the CPV and Si cell temperatures to be 77 °C and 56 °C with an uncertainty of ± 3 K when $V_{\mathrm{wind}} = 0$ m/s, $T_{\mathrm{amb}} = 25\,^{\circ}\mathrm{C}$, and GNI $= 1000$ W/m^2. Additionally, the obtained CPV array thermal resistance was found to be 30% larger than that of a conventional CPV module using a metal heatsink.

These findings demonstrate that silicon works as a heat distributing substrate if the total input power on the CPV cell is $<$2.8 W. This can either be achieved by limiting the concentration on the CPV cell or by applying smaller lenses and cells.

Acknowledgment

The authors would like to acknowledge SOITEC for the fabrication of four-junction solar cells and the Department III–V Photovoltaics and Concentrator Technology as well as the Module Technology Department at Fraunhofer ISE for their continuous support of this work. The authors are responsible for the content of this paper.

References

[1] F. Dimroth *et al.*, “Four-junction wafer-bonded concentrator solar cells,” *IEEE J. Photovolt.*, vol. 6, no. 1, pp. 343–349, Jan. 2016.
[2] S. P. Philipps and A. W. Bett, “III–V multi-junction solar cells,” in *Advanced Concepts in Photovoltaics (RSC Energy and Environment Series)*, vol. 11, A. J. Nozik, G. Conibeer, and M. C. Beard, Eds. London, U.K.: Roy. Soc. Chem., 2014, pp. 87–117.
[3] M. Steiner *et al.*, “43% Sunlight to electricity conversion efficiency using CPV,” *IEEE J. Photovolt.*, vol. 6, no. 4, pp. 1020–1024, Jul. 2016.
[4] G. Peharz, J. P. Ferrer-Rodríguez, G. Siefer, and A. W. Bett, “Investigations on the temperature dependence of CPV modules equipped with triple-junction solar cells,” *Prog. Photovolt., Res. Appl.*, vol. 90, no. 1, pp. 54–60, 2011.
[5] J. Jaus, R. Hue, M. Wiesenfarth, G. Peharz, and A. W. Bett, “Thermal management in a passively cooled concentrator photovoltaic module,” in *Proc. 23rd Eur. Photovolt. Sol. Energy Conf.*, Valencia, Spain, 2008, pp. 832–836.
[6] M. Wiesenfarth, S. Gamisch, H. Kraus, and A. W. Bett, “Investigations on 3-dimensional temperature distribution in a FLATCON-type CPV module,” in *Proc. 9th Int. Conf. Concentrator Photovolt. Syst.*, Miyazaki, Japan, 2013, pp. 189–193.
[7] Y. Ota, T. Sueto, H. Nagai, K. Araki, and K. Nishioka, “Reduction in operating temperature of 25 series-connected 820X concentrator photovoltaic module,” *Jpn. J. Appl. Phys.*, vol. 52, no. 4S, 2013, Art. no. 04CR03.
[8] K. Araki, H. Uozumi, and M. Yamaguchi, “A simple passive cooling structure and its heat analysis for 500× concentrator PV module,” in *Proc. Conf. Rec. 29th IEEE Photovolt. Spec. Conf.*, New Orleans, LA, USA, 2002, pp. 1568–1571.
[9] S. P. Philipps, A. W. Bett, K. Horowitz, and S. R. Kurtz, “Current status of concentrator photovoltaic (CPV) technology,” Nat. Renew. Energy Lab., Golden, CO, USA, 2017.
[10] M. Levinshtein, S. Rumyantsev, and M. Shur, Eds., *Si, Ge, C (Diamond), GaAs, GaP, GaSb, InAs, InP, InSb*. Singapore: World Scientific Publishing, 1996.
[11] PV Insights. [Online]. Available: http://pvinsights.com/. Accessed on: Jun. 11, 2018.
[12] K. Yoshikawa *et al.*, “Silicon heterojunction solar cell with interdigitated back contacts for a photoconversion efficiency over 26%,” *Nature Energy*, vol. 2, no. 5, 2017, Art. no. 17032.
[13] P. Benitez, J. C. Miñano, and R. Alvarez, “Photovoltaic concentrator with auxiliary cells collecting diffuse radiation,” U.S. Patent 2010/0126556 A1, May 27, 2010.
[14] M. Meitl, J. Carr, and K. Schneider, “Power augmentation in concentrator photovoltaic modules by collection of diffuse light,” U.S. Patent 2014/0261627 A1, Sep. 18, 2014.
[15] N. Yamada and K. Okamoto, “Experimental measurements of a prototype high concentration Fresnel lens CPV module for the harvesting of diffuse solar radiation,” *Opt. Express*, vol. 22, no. S1, A28–A34, 2014.
[16] N. Yamada and D. Hirai, “Maximization of conversion efficiency based on global normal irradiance using hybrid concentrator photovoltaic architecture,” *Prog. Photovolt., Res. Appl.*, vol. 24, no. 6, pp. 846–854, 2016.
[17] K.-T. Lee *et al.*, “Concentrator photovoltaic module architectures with capabilities for capture and conversion of full global solar radiation,” *Proc. Nat. Acad. Sci. USA*, vol. 113, no. 51, pp. E8210–E8218, 2016.
[18] J. Jaus, “Entwicklung von photovoltaischen Konzentratormodulen mit fresnel-linsen und reflektiver sekundäroptik,” Dissertation, Technische Fakultät, Albert-Ludwigs-Universität, Freiburg, Germany, 2009.
[19] k-Space Associates Inc., “Material properties.” [Online]. Available: https://www.k-space.com/support/material-properties/. Accessed on: Jun. 11, 2018.
[20] Ioffe Institute, “NSM archive-Physical properties of semiconductors.” [Online]. Available: http://www.ioffe.ru/SVA/NSM/Semicond/index.html. Accessed on: Jun. 11, 2018.
[21] P. Nitz, A. Heller, and W. Platzer, “Indoor characterization of Fresnel-type concentrator lenses,” in *Proc. 22nd Eur. Photovolt. Sol. Energy Conf. Exhib.*, Milan, Italy, 2007, pp. 289–293.
[22] I. M. Peters, Y. S. Khoo, and T. M. Walsh, “Detailed current loss analysis for a PV module made with textured multicrystalline silicon wafer solar cells,” *IEEE J. Photovolt.*, vol. 4, no. 2, pp. 585–593, Mar. 2014.
[23] J. H. I. Lienhard and J. H. V. Lienhard, *A Heat Transfer Textbook*, 1st ed. Cambridge, MA, USA: Phlogiston Press, 2008.
[24] C. Gueymard, *Simple Model of the Atmospheric Radiative Transfer of Sunshine (SMARTS2): Algorithms and Performance Assessment*. Cocoa, FL, USA: Florida Sol. Energy Center, 2009.
[25] F. J. Pern, “Ethylene-vinyl acetate (EVA) encapsulants for photovoltaic modules: Degradation and discoloration mechanisms and formulation modifications for improved photostability,” *Angew. Makromol. Chem.*, vol. 252, no. 1, pp. 195–216, 1997.
[26] M. Muller, S. R. Kurtz, M. Steiner, and G. Siefer, “Translating outdoor CPV I–V measurements to a CSTC power rating and the associated uncertainty,” *Prog. Photovolt., Res. Appl.*, vol. 23, pp. 1557–1571, 2015.
[27] D. Faiman, “Assessing the outdoor operating temperature of photovoltaic modules,” *Prog. Photovolt., Res. Appl.*, vol. 16, no. 4, pp. 307–315, 2008.
[28] G. Siefer and A. W. Bett, “Calibration of III–V concentrator cells and modules,” in *Proc. Conf. Rec. 4th World Conf. Photovolt. Energy Convers.*, Waikoloa, HI, USA, 2006, pp. 745–748.
[29] J. F. Martinez, M. Steiner, M. Wiesenfarth, and F. Dimroth, “4-terminal CPV module capable of converting global normal irradiance into electricity,” in *Proc. 14th Int. Conf. Concentrator Photovolt. Syst.*, Puertollano, Spain, 2018, pp. 090005-1–090005-7, doi: 10.1063/1.5053543.

Authors’ photographs and biographies not available at the time of publication.